CHAPTER 4

A KERNEL-FREE PARTICLE-FINITE ELEMENT METHOD FOR HYPERVELOCITY IMPACT SIMULATION

Young-Keun Park[1] **and Eric P. Fahrenthold**[2]

Department of Mechanical Engineering, 1 University Station C2200
University of Texas, Austin, TX 78712, USA

[1]Graduate student
[2]Professor, corresponding author, phone: (512) 471-3064, email: epfahren@mail.utexas.edu

A KERNEL FREE PARTICLE-FINITE ELEMENT METHOD FOR HYPERVELOCITY IMPACT SIMULATION

Young-Keun Park[3] and Eric P. Fahrenthold[4]

Department of Mechanical Engineering, 1 University Station C2200
University of Texas, Austin, TX 78712, USA

An improved hybrid particle-finite element method has been developed for the simulation of hypervelocity impact problems. Unlike alternative methods, the revised formulation computes the density without reference to any kernel or interpolation functions, for either the density or the rate of dilatation. This simplifies the state space model and leads to a significant reduction in computational cost. The improved method introduces internal energy variables as generalized coordinates in a new formulation of the thermomechanical Lagrange equations. Example problems show good agreement with exact solutions in one dimension and good agreement with experimental data in a three dimensional simulation.

KEYWORDS: particle methods, finite element methods, impact simulation

INTRODUCTION

Studies of hypervelocity impact phenomena are motivated by a variety of science and engineering applications [1]. Examples include scientific research on planetary impacts [2] and equations of state [3] and engineering research on the design of spacecraft shielding [4] and kinetic energy penetrators [5]. The proceedings of a recent international symposium [1] show that the use of computer simulation in this field is increasing, as improvements in numerical methods and computing power make it possible to address problems of greater complexity and larger scale. Simulation is of particular importance, as an adjunct to experimental work, when material costs are high [6] or when impact velocities beyond the range of light gas guns are of interest [7].

Simulation work in this field has applied a number of different numerical methods, based on continuum mechanics, particle dynamics, or mixed kinematic schemes. Continuum methods [8] employ either an Eulerian hydrodynamic [9,10] or a Lagrangian finite element [11]

---

[3]Graduate research assistant
[4]Professor, corresponding author, phone: (512) 471-3064, email: epfahren@mail.utexas.edu

approach, or some Arbitrary Lagrangian-Eulerian (ALE) based generalization of these techniques [12,13]. A large majority of particle codes employ a smooth particle hydrodynamics (SPH) technique [14,15,16], although some alternative particle based methods have been proposed [17]. Some disadvantages of pure continuum or pure particle based methods [18] have motivated the development of mixed continuum-particle formulations [4,19,20]. The most widely used mixed method is a coupled particle-finite element technique [19]. This technique initializes distinct material regions with either SPH particles or or Lagrangian finite elements, then quantifies subsequent material interactions using a particle-to-surface contact-impact algorithm. The alternative coupled particle-element method of Johnson and co-workers [20] maps damaged or failed elements into particles, and again quantifies particle-element interaction using a special contact algorithm. Both these methods are subject to tensile instability and numerical fracture problems.

The alternative mixed method of Fahrenthold and co-workers [21] is based on a hybrid particle-finite element formulation. This method in not subject to tensile instability and numerical fracture problems and eliminates the requirement for special treatment of particle-to-element contact-impact. It avoids both the mass diffusion problems of Eulerian methods and the mass and energy discard associated with Lagrangian element erosion algorithms. It is labeled a hybrid (versus coupled) method since it introduces both elements and particles for all material control volumes, then employs the elements and particles in tandem to represent distinct physics. The particles model all inertia, contact-impact, and thermomechanical response in compressed states, while the elements model tension and elastic-plastic shear. The method incorporates both ellipsoidal particles and time varying particle volumes and as a result can represent large density variations with relatively small neighbor counts. Previous work employing nonspherical evolving kernels has been rather limited and most particle simulations represent high densities using spherical particles, a fixed contact length, and relatively large neighbor sets.

The preceding formulation combines a true Lagrangian description of material strength

effects with a general particle based model of contact-impact dynamics, and has been validated in simulations of impact experiments conducted at velocities ranging from one to ten kilometers per second [22]. In the hypervelocity impact regime, where large strain plasticity, perforation, fragmentation, melting, and complex multi-structure contact-impact effects are often present, this formulation provides a particular combination of advantageous features not offered by alternative numerical methods. The present paper describes an improved hybrid particle-finite element method, modifying the formulation of Ravishankar and Fahrenthold [21] in two respects. First, the density is determined by integrating nonholonomic constraints imposed on the system level thermomechanical model. Second, the entropy states used previously to model the thermal domain are replaced by particle internal energies. These modifications simplify the method, reduce its computational cost, and incorporate equations of state expressed in standard functional form.

Unlike alternative methods, the revised formulation eliminates entirely the use of kernel or interpolation functions to represent the density or rate of dilatation fields. The density evolution equations are developed by direct reference to large deformation kinematics, avoiding any requirement to specify the functional dependence of an interaction potential on the particle coordinates. The latter task has proven to be quite difficult in an SPH context and is a principal focus of the general particle dynamics literature. The revised method introduces the use of internal energy variables as generalized coordinates in a new thermomechanical formulation of the discrete Lagrange equations. This avoids the requirement to construct Legendre transforms of the internal energy function, in order to express the dependence of pressure and temperature on entropy.

The present paper is organized as follows. First the particle and element kinematics are defined, followed by the kinetic co-energy and thermomechanical potential energy functions for the particle-element system. Second the evolution equations for the density are developed, followed by the evolution equations for the plastic and damage variables, all of these relations representing nonholonomic constraints on the system level model. Third the numerical

75

viscosity and numerical heat diffusion models are introduced, and evolution equations for the internal energy state variables are described, the latter states serving as generalized coordinates in a thermomechanical Lagrangian formulation. Fourth the discrete Lagrange equations for the particle-element system are derived, taking an explicit state space form convenient for numerical implementation. Finally application of the method is illustrated in one dimensional problems with exact solutions and in three dimensional simulations of representative hypervelocity impact problems.

PARTICLE KINEMATICS

The inertia of the modeled system is represented by a collection of n ellipsoidal particles, with $m^{(i)}$ the mass of particle i and $h_1^{(j)}, h_2^{(j)}, h_3^{(j)}$ the half-lengths of its major axes. The position and orientation of each particle is determined by its center of mass position vector ($\mathbf{c}^{(i)}$) and an Euler parameter [23,24] vector ($\mathbf{e}^{(i)}$)

$$\mathbf{c}^{(i)} = [\, c_1^{(i)} \; c_2^{(i)} \; c_3^{(i)} \,]^T, \qquad \mathbf{e}^{(i)} = [\, e_0^{(i)} \; e_1^{(i)} \; e_2^{(i)} \; e_3^{(i)} \,]^T \qquad (1)$$

where a superscript T denotes the transpose.

It is convenient to note here certain properties of Euler parameters, and to cite a number of well known [23] kinematic relations associated with their use. The Euler parameters provide a singularity free description of arbitrary particle rotations. They define a rotation matrix ($\mathbf{R}^{(i)}$) for each particle

$$\mathbf{R}^{(i)} = \mathbf{A}^{(i)} \, \mathbf{G}^{(i)T} \qquad (2)$$

$$\mathbf{A}^{(i)} = \begin{bmatrix} -e_1^{(i)} & e_0^{(i)} & -e_3^{(i)} & e_2^{(i)} \\ -e_2^{(i)} & e_3^{(i)} & e_0^{(i)} & -e_1^{(i)} \\ -e_3^{(i)} & -e_2^{(i)} & e_1^{(i)} & e_0^{(i)} \end{bmatrix} \qquad (3)$$

$$\mathbf{G}^{(i)} = \begin{bmatrix} -e_1^{(i)} & e_0^{(i)} & e_3^{(i)} & -e_2^{(i)} \\ -e_2^{(i)} & -e_3^{(i)} & e_0^{(i)} & e_1^{(i)} \\ -e_3^{(i)} & e_2^{(i)} & -e_1^{(i)} & e_0^{(i)} \end{bmatrix} \qquad (4)$$

which relates vector components $\mathbf{v}$ described in a fixed global Cartesian coordinate system to corresponding components $\hat{\mathbf{v}}$ described in a co-rotating system aligned with the particle major axes, using

$$\mathbf{v} = \mathbf{R}^{(i)}\,\hat{\mathbf{v}} \tag{5}$$

The Euler parameters and their time derivatives are related to the angular velocity vector of the particle ($\boldsymbol{\omega}^{(i)}$), described in the co-rotating frame, by

$$\dot{\mathbf{e}}^{(i)} = \frac{1}{2}\,\mathbf{G}^{(i)T}\,\boldsymbol{\omega}^{(i)} \tag{6}$$

Similarly the antisymmetric matrix $\boldsymbol{\Omega}^{(i)}$ with axial vector $\boldsymbol{\omega}^{(i)}$, which satisfies

$$\boldsymbol{\Omega}^{(i)}\mathbf{v} = \boldsymbol{\omega}^{(i)} \times \mathbf{v} \tag{7}$$

for all vectors $\mathbf{v}$, is related to the Euler parameters and their time derivatives by the relations

$$\boldsymbol{\Omega}^{(i)} = 2\,\mathbf{G}^{(i)}\,\dot{\mathbf{G}}^{(i)T} = -2\,\dot{\mathbf{G}}^{(i)}\mathbf{G}^{(i)T} = \mathbf{R}^{(i)T}\,\dot{\mathbf{R}}^{(i)} \tag{8}$$

For ellipsoidal particles it is convenient to describe the separation distance of the mass centers for particles i and j using the ellipsoidal coordinate

$$\zeta^{(i,j)} = \left[\left(\mathbf{c}^{(i)} - \mathbf{c}^{(j)}\right)^{T}\hat{\mathbf{H}}^{(j)}\left(\mathbf{c}^{(i)} - \mathbf{c}^{(j)}\right)\right]^{\frac{1}{2}} \tag{9}$$

defined in the co-rotating system of particle j using

$$\hat{\mathbf{H}}^{(j)} = \mathbf{R}^{(j)}\mathbf{H}^{(j)}\mathbf{R}^{(j)T} \tag{10}$$

$$\mathbf{H}^{(j)} = \begin{bmatrix} 2\beta h_1^{(j)} & 0 & 0 \\ 0 & 2\beta h_2^{(j)} & 0 \\ 0 & 0 & 2\beta h_3^{(j)} \end{bmatrix}^{-2} \tag{11}$$

where the constant β allows for close packing at the reference density. The time derivative of this ellipsoidal coordinate , defined for $i \neq j$, is

$$\dot{\zeta}^{(i,j)} = \frac{1}{\zeta^{(i,j)}}\left[\left(\hat{\mathbf{H}}^{(j)}\mathbf{r}^{(i,j)}\right)^{T}\dot{\mathbf{r}}^{(i,j)} + \left(\mathbf{H}^{(j)}\hat{\mathbf{r}}^{(i,j)} \times \hat{\mathbf{r}}^{(i,j)}\right)^{T}\boldsymbol{\omega}^{(j)}\right] \tag{12}$$

where

$$\mathbf{r}^{(i,j)} = \mathbf{c}^{(i)} - \mathbf{c}^{(j)}, \qquad \hat{\mathbf{r}}^{(i,j)} = \mathbf{R}^{(j)T}\mathbf{r}^{(i,j)} \tag{13}$$

and may be used to quantify the rate of compression for an array of ellipsoidal particles.

The preceding results will be used in later sections to account for rotational inertia and particle kinematics not present in the vast majority of particle models, which assume a spherical particle geometry.

FINITE ELEMENT KINEMATICS

This section describes the finite element kinematics employed in the present paper. The elements used here are eight noded hexahedra, well known and described in detail by Hallquist [11] and others. Since all inertia effects are represented by the particles, no mass matrix is defined.

Each structure in the model is subdivided into uniform hexahedra with orthogonal faces, with ellipsoidal particles located at each node and at the centroid of each element. The center of mass coordinates for particles located at element vertices are also nodal coordinates for the hexahedra, and are used to compute the shearing strain. The center of mass coordinates for particles located at the element centroids are used, in combination with the nodal coordinates, to define six subelements for each hexahedron. The volumes of these subelements are used to compute interparticle tension forces.

The following Lagrangian finite strain deformation measures [25] are used in the stored energy functions for the elements, associated with tension and shear, and in the plastic constitutive relations. The shear strain for element j is

$$\overline{\mathbf{E}}^{(j)} = \frac{1}{2}\left(\overline{\mathbf{C}}^{(j)} - \mathbf{I} \right) \tag{14}$$

where

$$\overline{\mathbf{C}}^{(j)} = \overline{\mathbf{F}}^{(j)T}\overline{\mathbf{F}}^{(j)}, \qquad \overline{\mathbf{F}}^{(j)} = \left(det\,\mathbf{F}^{(j)} \right)^{-\frac{1}{3}} \mathbf{F}^{(j)} \tag{15}$$

and $\mathbf{F}^{(j)}$ is an element deformation gradient computed using one point integration [11]. The

elastic shear strain is defined as

$$\mathbf{E}^{e(j)} = \overline{\mathbf{E}}^{(j)} - \mathbf{E}^{p(j)} \tag{16}$$

where $(\mathbf{E}^{p(j)})$ is a plastic stain tensor whose flow rule satisfies the isochoric plastic deformation constraint

$$tr\left(\mathbf{C}^{p(j)-T}\dot{\mathbf{C}}^{p(j)}\right) = 0, \qquad \mathbf{E}^{p(j)} = \frac{1}{2}\left(\mathbf{C}^{p(j)} - \mathbf{I}\right) \tag{17}$$

The subelement Jacobians are denoted by $J^{(j,k)}$, where the index k designates one of six subelements for the jth hexahedron.

KINETIC CO-ENERGY AND POTENTIAL ENERGY

An energy method (Lagrange's equations) is adopted here, to facilitate the systematic integration of diverse particle and element based modeling concepts. The stored energy functions considered here are a kinetic co-energy function for the particles, an internal energy function for the particles, and element potential energy functions which account for tension and shear. Damage variables are introduced to model element failure in a thermodynamically consistent fashion. Constitutive assumptions different from those adopted here may be introduced without change to the underlying methodology.

The system kinetic co-energy is the sum of the particle co-energies

$$T^* = \sum_{i=1}^{n} T^{*(i)} \tag{18}$$

where $T^{*(i)}$ is the co-energy for particle i, due to translation and rotation

$$T^{*(i)} = \frac{1}{2}m^{(i)}\dot{\mathbf{c}}^{(i)\,T}\dot{\mathbf{c}}^{(i)} + \frac{1}{2}\boldsymbol{\omega}^{(i)\,T}\mathbf{J}^{(i)}\boldsymbol{\omega}^{(i)} \tag{19}$$

with $\mathbf{J}^{(i)}$ a constant moment of inertia matrix described in the co-rotating particle frame. The system kinetic co-energy function defines the generalized momenta

$$\mathbf{p}^{(i)} = \frac{\partial T^*}{\partial \dot{\mathbf{c}}^{(i)}} = m^{(i)}\dot{\mathbf{c}}^{(i)}, \qquad \mathbf{h}^{(i)} = \frac{\partial T^*}{\partial \boldsymbol{\omega}^{(i)}} = \mathbf{J}^{(i)}\boldsymbol{\omega}^{(i)} \tag{20}$$

where $\mathbf{p}^{(i)}$ and $\mathbf{h}^{(i)}$ are translational and angular momentum vectors for the ith particle.

The system potential energy has the general form

$$V = \sum_{i=1}^{n} U^{(i)} + \sum_{j=1}^{n_e} V_o^{e(j)} \, \psi^{(j)} + \sum_{j=1}^{n_e} \sum_{k=1}^{n_s} V_o^{e(j,k)} \, \psi^{(j,k)} \tag{21}$$

where $U^{(i)}$ is the total internal energy for particle i and the pressure $(P^{(i)})$ and temperature $(\theta^{(i)})$ are described by an equation of state [26] with functional form

$$P^{(i)} = P^{(i)}(\rho^{(i)}, u^{(i)}), \qquad \theta^{(i)} = \theta^{(i)}(\rho^{(i)}, u^{(i)}) \tag{22}$$

with $\rho^{(i)}$ and $u^{(i)}$ the density and the internal energy per unit mass

$$u^{(i)} = \frac{U^{(i)}}{m^{(i)}} \tag{23}$$

The second term depends on the number of elements (n_e), the reference volume $(V_o^{e(j)})$ for element j, and the strain energy per unit volume in shear $(\psi^{(j)})$, here assumed to be

$$\psi^{(j)} = \left(1 - d^{(j)}\right) \mu^{(j)} \, tr \left(\mathbf{E}^{e(j)T} \mathbf{E}^{e(j)}\right) \tag{24}$$

where $d^{(j)}$ is a shear damage variable and $\mu^{(j)}$ is a shear modulus. The third term depends on the number of subelements per element (n_s), the subelement reference volumes $(V_o^{e(j,k)})$, and the strain energy per unit volume in tension $(\psi^{(j,k)})$, here assumed to be

$$\psi^{(j,k)} = \frac{1}{2} \left(1 - D^{(j)}\right) K^{(j)} \, < J^{(j,k)} - 1 >^2 \tag{25}$$

where $D^{(j)}$ is a normal damage variable, $K^{(j)}$ is a bulk modulus, $< x >$ denotes the bracket function

$$< x > = \, x \, \hat{u}(x) \tag{26}$$

and $\hat{u}$ denotes the unit step function. Since the subelement Jacobians and the shear strain tensor depend on the particle center of mass coordinates

$$J^{(j,k)} = J^{(j,k)} \left(\mathbf{c}^{(i)}\right), \qquad \mathbf{E}^{e(j)} = \mathbf{E}^{e(j)} \left(\mathbf{c}^{(i)}, \mathbf{E}^{p(j)}\right) \tag{27}$$

it follows that the system potential energy has the general functional form

$$V = V \left(\rho^{(i)}, U^{(i)}, \mathbf{c}^{(i)}, d^{(j)}, D^{(j)}, \mathbf{E}^{p(j)}\right) \tag{28}$$

The system potential energy defines the generalized conservative forces

$$m^{(i)} \frac{P^{(i)}}{\rho^{(i)2}} = \frac{\partial V}{\partial \rho^{(i)}}, \qquad \mathbf{g}^{(i)} = \frac{\partial V}{\partial \mathbf{c}^{(i)}}, \qquad 1 = \frac{\partial V}{\partial U^{(i)}} \tag{29}$$

as well as the deviatoric stress

$$\mathbf{S}^{(j)} = -\frac{1}{V_o^{e(j)}} \frac{\partial V}{\partial \mathbf{E}^{p(j)}} \tag{30}$$

and the strain energy release rates

$$\Gamma^{D(j)} = -\frac{\partial V}{\partial D^{(j)}}, \qquad \Gamma^{d(j)} = -\frac{\partial V}{\partial d^{(j)}} \tag{31}$$

due to damage evolution. Note that when the internal energy is introduced as a generalized coordinate, the associated generalized forces are constant.

With the system Lagrangian now defined, the next four sections describe evolution equations for the internal state variables.

DENSITY EVOLUTION RELATIONS

This section derives density evolution relations for the particles, by extending certain exact results for the deformation kinematics of a unit cell of spherical particles, arranged in a body centered cubic packing scheme. For uniform compression of such a unit cell, in isolation, the cell center density $\rho^{(i)}$ is related to the reference density $\rho_o^{(i)}$, the center of mass separation distances $r^{(i,j)}$ and particle radii $h^{(j)}$ for its eight neighbors by

$$\frac{\rho^{(i)}}{\rho_o^{(i)}} = 1 + \frac{1}{8} \sum_{j=1}^{8} \left[\left(\frac{2\beta h^{(j)}}{r^{(i,j)}} \right)^3 - 1 \right] \tag{32}$$

If the particles are not spherical but ellipsoidal then

$$\frac{\rho^{(i)}}{\rho_o^{(i)}} = 1 + \frac{1}{8} \sum_{j=1}^{8} \left[\left(\frac{1}{\zeta^{(i,j)}} \right)^3 - 1 \right] \tag{33}$$

This expression for an isolated cell may be extended to a cell array of arbitrary size by describing the same kinematics in rate form. Taking the time derivative of the last equation

and multiplying by a step function $W^{(i,j)}$ which allows for contact with near neighbors only yields

$$\frac{\dot{\rho}^{(i)}}{\rho_o{}^{(i)}} = -\frac{3}{8} \sum_{j=1}^{n} \frac{\dot{\zeta}^{(i,j)}}{\zeta^{(i,j)4}} W^{(i,j)} \tag{34}$$

where the summation is now over all n particles. The coefficient $W^{(i,j)}$ must satisfy

$$W^{(i,j)} = \begin{cases} 0 & \text{if } i = j \\ 0 & \text{if } i \neq j \text{ and } \zeta^{(i,j)3} \geq \frac{\rho_o^{(i)}}{\rho^{(i)}} \\ 1 & \text{if } i \neq j \text{ and } \zeta^{(i,j)3} < \frac{\rho_o^{(i)}}{\rho^{(i)}} \end{cases}$$

in order to correctly reflect the dependence of particle contact distance on the local density. Otherwise particles will contact remote neighbors through intervening matter. Hence

$$W^{(i,j)} = (1 - \delta_{ij}) \, \hat{u} \left(1 - \zeta^{(i,j)} \left[\frac{\rho^{(j)}}{\rho_o{}^{(j)}} \right]^{1/3} \right) \tag{35}$$

where δ_{ij} denotes the Kronecker delta. Note that $W^{(i,j)}$ performs no interpolation. Introducing the kinematic relation for $\dot{\zeta}^{(i,j)}$, developed in an earlier section, yields

$$\dot{\rho}^{(i)} = -\frac{3}{8} \sum_{j=1}^{n} \rho_o{}^{(i)} \frac{W^{(i,j)}}{\zeta^{(i,j)5}} \left[\left(\hat{\mathbf{H}}^{(j)} \mathbf{r}^{(i,j)} \right)^T \dot{\mathbf{r}}^{(i,j)} + \left(\mathbf{H}^{(j)} \hat{\mathbf{r}}^{(i,j)} \times \hat{\mathbf{r}}^{(i,j)} \right)^T \boldsymbol{\omega}^{(j)} \right] \tag{36}$$

which is the constraint form of the density evolution relations. The coefficients of the particle translational velocities and angular velocities in this expression will determine generalized forces in the momentum balance (Lagrange) equations derived in a later section. When the particle velocities in this expression are eliminated in favor of the particle momenta

$$\dot{\mathbf{c}}^{(i)} = m^{(i)-1} \mathbf{p}^{(i)}, \qquad \boldsymbol{\omega}^{(i)} = \mathbf{J}^{(i)-1} \mathbf{h}^{(i)} \tag{37}$$

the density evolution equations take an explicit state space form convenient for use in numerical simulation.

PLASTICITY AND DAMAGE MODELS

This section introduces evolution equations for the plastic and damage variables. As in the case of the potential energy, alternative constitutive assumptions may be introduced without

change to the basic modeling methodology. The plastic flow rule used here is adapted from reference [27], and represents the simplest possible accommodation of the aforementioned isochoric plastic deformation constraint. The flow rule is

$$\dot{\mathbf{E}}^{p(j)} = \frac{\dot{\lambda}^{(j)}}{||S^{p(j)}||} \, \underline{\underline{\mathbf{N}}}^{p(j)} \, \underline{\underline{\mathbf{N}}} \, \mathbf{S}^{p(j)} \tag{38}$$

where $\dot{\lambda}^{(j)}$ is a positive proportionality coefficient, $\mathbf{S}^{p(j)}$ is an effective stress

$$\mathbf{S}^{p(j)} = \underline{\underline{\mathbf{N}}}^T \, \underline{\underline{\mathbf{N}}}^{p(j)T} \, \mathbf{S}^{(j)} \tag{39}$$

and the invariant operator is defined by

$$||\mathbf{T}|| = \left[\frac{1}{2} \, tr \left(\mathbf{T}^T \mathbf{T} \right) \right]^{1/2} \tag{40}$$

for any second order tensor $\mathbf{T}$. The fourth order tensor coefficients in the flow rule are defined by

$$\underline{\underline{\mathbf{N}}}^{p(j)} \, \mathbf{T} = \frac{1}{2 \, ||C^{p(j)}||} (\mathbf{C}^{p(j)} \, \mathbf{T} + \mathbf{T} \, \mathbf{C}^{p(j)}) \tag{41}$$

$$\underline{\underline{\mathbf{N}}} \, \mathbf{T} = \mathbf{T} - \frac{1}{3} tr(\mathbf{T}) \, \mathbf{I} \tag{42}$$

for any symmetric second order tensor $\mathbf{T}$. The yield function is

$$f^{(j)} = ||S^{p(j)}|| - Y^{(j)} \tag{43}$$

where $Y^{(j)}$ is the yield stress

$$Y^{(j)} = Y_o^{(j)} \, (1 - d^{(j)}) \, (1 + \kappa^{(j)} \epsilon^{p(j)})^{\alpha^{(j)}} \, \left(1 - \eta^{(j)} \theta^{H(j)} \right) \tag{44}$$

with $\epsilon^{p(j)}$ the effective plastic strain, $\kappa^{(j)}$ a strain hardening coefficient, $\alpha^{(j)}$ a strain hardening exponent, $\eta^{(j)}$ a thermal softening coefficient, and $\theta^{H(j)}$ the homologous temperature. The effective plastic strain is determined by integrating the rate relation

$$\dot{\epsilon}^{p(j)} = ||\dot{\mathbf{E}}^{p(j)}|| \tag{45}$$

while the incremental plastic strain for a time step Δt is computed using

$$\Delta\lambda^{(j)} = \frac{<||S^{p(j)}|| - Y^{(j)}>}{(1 - d^{(j)})\,2\,\mu^{(j)}} \tag{46}$$

The damage evolution equations applied here are adapted from reference [28], and dissipate the strain energy stored in tension and shear over $\hat{n}$ time steps, once an element meets any stipulated material failure criteria. The evolution equations are

$$\dot{D}^{(j)} = \frac{\Lambda^{(j)}}{\hat{n}\,\Delta t}\,\hat{u}(1 - D^{(j)}), \qquad \dot{d}^{(j)} = \frac{\Lambda^{(j)}}{\hat{n}\,\Delta t}\,\hat{u}(1 - d^{(j)}) \tag{47}$$

where $\Lambda^{(j)}$ is initialized to zero, and is set to a value of one when the accumulated plastic strain, temperature, or element compression reach corresponding critical values for the plastic failure strain ($\epsilon_f^{p(j)}$), melt temperature ($\theta_m^{(j)}$), or maximum compression ($J_c^{(j)}$). Other failure criteria may of course be specified.

In general terms, the plastic and damage evolution equations are noholonomic constraints of the form

$$\dot{\mathbf{E}}^{p(j)} = \dot{\mathbf{E}}^{p(j)}\left(\rho^{(i)}, U^{(i)}, \mathbf{c}^{(i)}, d^{(j)}, D^{(j)}, \epsilon^{p(j)}, \mathbf{E}^{p(j)}\right) \tag{48}$$

$$\dot{d}^{(j)} = \dot{d}^{(j)}\left(\rho^{(i)}, U^{(i)}, \mathbf{c}^{(i)}, d^{(j)}, D^{(j)}, \epsilon^{p(j)}, \mathbf{E}^{p(j)}\right) \tag{49}$$

$$\dot{D}^{(j)} = \dot{D}^{(j)}\left(\rho^{(i)}, U^{(i)}, \mathbf{c}^{(i)}, d^{(j)}, D^{(j)}, \epsilon^{p(j)}, \mathbf{E}^{p(j)}\right) \tag{50}$$

on the system level Lagrangian model.

ARTIFICIAL VISCOSITY AND HEAT DIFFUSION

Shock physics codes of the continuum or particle type incorporate a numerical viscosity and artificial heat diffusion. The forms used here are typical of particle codes, with one exception. Since the ellipsoidal particles used here admit rotational degrees of freedom, a viscous torque has been added which damps the relative rotation of neighboring particles.

A viscous force is introduced for converging particles only

$$\mathbf{f}^{(i)} = \sum_{j=1}^{n} \nu^{(i,j)}\,max\left(0, v^{(i,j)}\right) \frac{\left(\mathbf{c}^{(i)} - \mathbf{c}^{(j)}\right)}{|\,\mathbf{c}^{(i)} - \mathbf{c}^{(j)}\,|}\,\hat{u}(1 - \zeta^{(i,j)}) \tag{51}$$

where the relative normal velocity is

$$v^{(i,j)} = -\left(\dot{\mathbf{c}}^{(i)} - \dot{\mathbf{c}}^{(j)} \right) \cdot \frac{\left(\mathbf{c}^{(i)} - \mathbf{c}^{(j)} \right)}{|\, \mathbf{c}^{(i)} - \mathbf{c}^{(j)} \,|} \tag{52}$$

and the viscosity coefficient is

$$\nu^{(i,j)} = \frac{c_o}{2} \left(\rho_o^{(i)} \, c_s^{(i)} V_o^{(i)\frac{2}{3}} + \rho_o^{(j)} \, c_s^{(j)} V_o^{(j)\frac{2}{3}} \right) \left[1 + \frac{2\, c_1 |v^{(i,j)}|}{(c_s^{(i)} + c_s^{(j)})} \right] \tag{53}$$

with $c_s^{(i)}$ and $V_o^{(i)}$ a soundspeed and particle reference volume. The parameters c_o and c_1 are nondimensional linear and quadratic numerical viscosity coefficients.

Similarly the viscous torque is

$$\mathbf{M}^{(i)} = \sum_{j=1}^{n} \sigma^{(i,j)} \, \mathbf{R}^{(i)T} \left(\mathbf{R}^{(i)} \boldsymbol{\omega}^{(i)} - \mathbf{R}^{(j)} \boldsymbol{\omega}^{(j)} \right) \hat{u}(1 - \zeta^{(i,j)}) \tag{54}$$

where the torsional damping coefficient is

$$\sigma^{(i,j)} = \frac{c_o}{2} \left(\rho_o^{(i)} \, c_s^{(i)} V_o^{(i)\frac{4}{3}} + \rho_o^{(j)} \, c_s^{(j)} V_o^{(j)\frac{4}{3}} \right) \tag{55}$$

Finally the thermal power flow due to artificial heat diffusion is taken to be

$$\dot{Q}^{con(i)} = \sum_{j=1}^{n} R^{(i,j)} \left(\theta^{(i)} - \theta^{(j)} \right) \hat{u}(1 - \zeta^{(i,j)}) \tag{56}$$

where the heat transfer coefficient is

$$R^{(i,j)} = \frac{k_o}{2} \left(\rho_o^{(i)} \, c_s^{(i)} c_v^{(i)} V_o^{(i)\frac{2}{3}} + \rho_o^{(j)} \, c_s^{(j)} c_v^{(j)} V_o^{(j)\frac{2}{3}} \right) \tag{57}$$

with $c_v^{(i)}$ a specific heat and k_o a numerical heat diffusion coefficient.

INTERNAL ENERGY EVOLUTION EQUATIONS

The last internal state variable to be considered is the internal energy. The introduction of internal energy states as generalized coordinates allows the thermomechanical problem of interest here to be solved using energy methods.

The internal energy evolution equations for particle i are

$$\dot{U}^{(i)} = \dot{U}^{wrk(i)} + \dot{U}^{irr(i)} - \dot{U}^{con(i)} \tag{58}$$

where the first term accounts for mechanical work, the second term accounts for the effects of irreversible entropy production, and the third term represents numerical heat diffusion.

The mechanical power flow for particle i is

$$\dot{U}^{wrk(i)} = m^{(i)} \frac{P^{(i)}}{\rho^{(i)2}} \dot{\rho}^{(i)} \tag{59}$$

The energy dissipation due to irreversible entropy production for particle i depends on the viscous forces and torques, which act on the particles, and on the dissipation in the elements

$$\dot{U}^{irr(i)} = \mathbf{f}^{(i)T}\dot{\mathbf{c}}^{(i)} + \mathbf{M}^{(i)T}\boldsymbol{\omega}^{(i)} + \sum_{j=1}^{n} \phi^{(i,j)} \dot{Q}^{irr(j)} \tag{60}$$

where $\dot{Q}^{irr(j)}$ is a power flow due to damage evolution and plastic deformation in element j

$$\dot{Q}^{irr(j)} = \Gamma^{D(j)}\dot{D}^{(j)} + \Gamma^{d(j)}\dot{d}^{(j)} + V_o^{e(j)} \, tr\left(\mathbf{S}^{(j)T}\dot{\mathbf{E}}^{p(j)}\right) \tag{61}$$

and $\phi^{(i,j)}$ is the fraction of the dissipation in element j associated with particle i.

Finally the internal energy flows due to numerical heat diffusion are

$$\dot{U}^{con(i)} = \dot{Q}^{con(i)} \tag{62}$$

As in the case of the density evolution equations, a constraint form of the internal evolution relations is used to identify the generalized forces which appear in the Lagrange equations developed in the next section. For numerical implementation of the method, the generalized velocities are eliminated by introducing the momentum states as well as evolution relations for the density, plastic, and damage state variables. The resulting internal energy evolution relations take an explicit state space form.

LAGRANGE'S EQUATIONS

The preceding sections defined stored energy functions and nonholonomic constraints for the thermomechanical particle-element system. This section develops the final ODE model. The results of Shivarama and Fahrenthold [21] allow in the present case Lagrange's equations

to take the canonical form

$$\dot{\mathbf{p}}^{(i)} = -\mathbf{g}^{(i)} + \mathbf{q}^{c(i)}, \qquad \dot{\mathbf{c}}^{(i)} = m^{(i)-1}\,\mathbf{p}^{(i)} \tag{63}$$

$$\dot{\mathbf{h}}^{(i)} = -\mathbf{\Omega}^{(i)}\mathbf{h}^{(i)} + \mathbf{Q}^{c(i)}, \qquad \dot{\mathbf{e}}^{(i)} = \frac{1}{2}\mathbf{G}^{(i)T}\mathbf{J}^{(i)-1}\mathbf{h}^{(i)} \tag{64}$$

$$\frac{\partial V}{\partial \rho^{(i)}} = Q^{\rho(i)}, \qquad \frac{\partial V}{\partial U^{(i)}} = Q^{U(i)} \tag{65}$$

$$\frac{\partial V}{\partial d^{(j)}} = Q^{d(j)}, \qquad \frac{\partial V}{\partial D^{(j)}} = Q^{D(j)}, \qquad \frac{\partial V}{\partial \mathbf{E}^{p(j)}} = \mathbf{Q}^{p(j)} \tag{66}$$

where $\mathbf{q}^{c(i)}$, $\mathbf{Q}^{c(i)}$, $\mathbf{Q}^{\rho(i)}$, $Q^{U(i)}$, $Q^{d(i)}$, $Q^{D(i)}$, and $\mathbf{Q}^{p(j)}$ are generalized forces determined by the nonholonomic constraints. The degenerate forms of the Lagrange equations for the internal state variables are due to the fact that those variables are not associated with any generalized momenta. Introducing Lagrange multipliers $\gamma^{\rho(i)}$, $\gamma^{U(i)}$, $\gamma^{d(j)}$, $\gamma^{D(j)}$, and $\mathbf{X}^{p(j)}$ for the constraints, the generalized forces are found to be

$$\mathbf{q}^{c(i)} = -\gamma^{U(i)}\,\mathbf{f}^{(i)} + \frac{3}{8}\sum_{j=1}^{n}\left[\gamma^{\rho(i)}\rho_o^{(i)}\frac{W^{(i,j)}}{\zeta^{(i,j)5}}\hat{\mathbf{H}}^{(j)}\mathbf{r}^{(i,j)} - \gamma^{\rho(j)}\rho_o^{(j)}\frac{W^{(j,i)}}{\zeta^{(j,i)5}}\hat{\mathbf{H}}^{(i)}\mathbf{r}^{(j,i)}\right] \tag{67}$$

$$\mathbf{Q}^{c(i)} = -\gamma^{U(i)}\,\mathbf{M}^{(i)} + \frac{3}{8}\sum_{j=1}^{n}\gamma^{\rho(j)}\rho_o^{(j)}\frac{W^{(j,i)}}{\zeta^{(j,i)5}}\left(\mathbf{H}^{(i)}\hat{\mathbf{r}}^{(j,i)} \times \hat{\mathbf{r}}^{(j,i)}\right) \tag{68}$$

$$Q^{\rho(i)} \;=\; \gamma^{\rho(i)} \tag{69}$$

$$Q^{U(i)} \;=\; \gamma^{U(i)} \tag{70}$$

$$Q^{d(j)} \;=\; \gamma^{d(j)} - \sum_{i=1}^{n}\gamma^{U(i)}\,\phi^{(i,j)}\,\Gamma^{d(j)} \tag{71}$$

$$Q^{D(j)} \;=\; \gamma^{D(j)} - \sum_{i=1}^{n}\gamma^{U(i)}\,\phi^{(i,j)}\,\Gamma^{D(j)} \tag{72}$$

$$\mathbf{Q}^{p(j)} \;=\; \mathbf{X}^{p(j)} - \sum_{i=1}^{n}\gamma^{U(i)}\,\phi^{(i,j)}\,V_o^{(j)}\,\mathbf{S}^{(j)} \tag{73}$$

87

These results allow the unknown Lagrange multipliers to be determined in closed form, so that the final Lagrange equations are

$$\dot{\mathbf{p}}^{(i)} = -\mathbf{g}^{(i)} - \mathbf{f}^{(i)} + \mathbf{q}^{(i)} \tag{74}$$

$$\dot{\mathbf{h}}^{(i)} = -\mathbf{\Omega}^{(i)}\mathbf{h}^{(i)} - \mathbf{M}^{(i)} + \mathbf{Q}^{(i)} \tag{75}$$

$$\dot{\mathbf{c}}^{(i)} = m^{(i)-1}\mathbf{p}^{(i)} \tag{76}$$

$$\dot{\mathbf{e}}^{(i)} = \frac{1}{2}\mathbf{G}^{(i)T}\mathbf{J}^{(i)-1}\mathbf{h}^{(i)} \tag{77}$$

where the generalized forces and torques due to particle interactions are

$$\mathbf{q}^{(i)} = \frac{3}{8}\sum_{j=1}^{n}\left(V_o^{(i)}\frac{P^{(i)}}{\rho^{(i)2}}\frac{W^{(i,j)}}{\zeta^{(i,j)5}}\hat{\mathbf{H}}^{(j)} + V_o^{(j)}\frac{P^{(j)}}{\rho^{(j)2}}\frac{W^{(j,i)}}{\zeta^{(j,i)5}}\hat{\mathbf{H}}^{(i)}\right)\mathbf{r}^{(i,j)} \tag{78}$$

$$\mathbf{Q}^{(i)} = \frac{3}{8}\sum_{j=1}^{n}V_o^{(j)}\frac{P^{(j)}}{\rho^{(j)2}}\frac{W^{(j,i)}}{\zeta^{(j,i)5}}\left(\mathbf{H}^{(i)}\hat{\mathbf{r}}^{(j,i)} \times \hat{\mathbf{r}}^{(j,i)}\right) \tag{79}$$

Supplemented by the evolution equations for density, internal energy, shear damage, normal damage, and plastic strain, the result is an explicit first order ODE model for the thermo-mechanical particle-element system.

EXAMPLE SIMULATIONS

This section describes four example problems which illustrate application of the improved particle-element method developed in this paper. The first two examples involve one dimensional test problems with known exact solutions. The third and fourth example problems involve three dimensional simulations. The third example models a published experiment while the fourth example measures the relative computational cost of the present method in a hypervelocity impact application of current research interest.

The first example is the wall shock problem of Noh [31]. The simulations employ an ideal gas equation of state

$$P = (\gamma - 1)\,\rho\,(u - u_o), \qquad \theta = \frac{1}{c_v}\,(u - u_o) \tag{80}$$

and the parameters shown in Table 1. This problem models the collision of a fluid stream located initially in the region $0.0 < x < 0.5$ with a rigid wall located at $x = 0$. The initial conditions are $\rho = \rho_o$, $u = u_o$, and $v = -1$. Figures 1 through 4 plot the simulation results for velocity, density, pressure, and temperature at the stop time of 0.3, for a model composed of 200 particles. The numerical results show good agreement with the exact solution, although better results have been obtained using finite difference and finite element methods [31,35]. Table 2 shows convergence of the simulation results, as the particle count is increased, in terms of the velocity error norm

$$\| e \|_v = \left\{ \frac{1}{n} \sum_{i=1}^{n} \left[v^{(i)} - \hat{v}(x^{(i)}) \right]^2 \right\}^{1/2} \tag{81}$$

and the temperature error norm

$$\| e \|_\theta = \left\{ \frac{1}{n} \sum_{i=1}^{n} \left[\theta^{(i)} - \hat{\theta}(x^{(i)}) \right]^2 \right\}^{1/2} \tag{82}$$

where $\hat{v}$ and $\hat{\theta}$ denote the exact solutions for the velocity and temperature.

The second example is the bar impact problem of Kolsky [33]. The simulations employ a linear isothermal equation of state

$$P = K \left(\rho/\rho_0 - 1 \right) \tag{83}$$

and the parameters shown in Table 3. This problem models the one dimensional motion of an elastic bar of length L subjected to a step tensile pressure loading of magnitude P_{ext}, applied at the end $x = L$ at time $t = 0$. Figures 5 and 6 plot the simulation results for the bar midpoint velocity versus time, to a stop time of 0.001 seconds, for two different particle counts. The numerical results show good agreement with the exact solution. The results shown in Figure 5 are quite similar to those reported by Lu et a. [34], at the same particle count, employing an element-free Galerkin method with an explicit integration algorithm.

The third example problem models the oblique impact of a tungsten alloy (DX2HCMF) rod on a steel (SIS 2541) plate, an experiment described in references [29] and [30]. The

89

simulations employed a Mie-Gruneisen equation of state [32] and the material properties [30,32] listed in Table 4. The cylindrical projectile has a diameter of 0.5 cm and a length of 7.5 cm (L/D = 15). The simulation models a 1.5 km/s impact on a 0.5 cm thick plate at a sixty degree obliquity, and was run at three different particle counts. Figures 7 and 8 show the initial configuration and the simulation results at 100 microseconds after impact, while Figures 9 and 10 show sectioned views at 20 and 40 microseconds after impact. This simulation illustrates the fact that the present method retains all material fragments and models contact-impact of all intact and fragmented material. Table 5 provides simulation results, at several particle counts, for the residual rod length and residual rod velocity, showing good agreement with the corresponding experimental values (6.38 cm and 1.46 km/s). The simulation results shown here differ by less than three percent from those reported by Lee and Yoo [30] for Lagrangian finite element methods.

The fourth example problem models the oblique impact of an aluminum sphere on a reinforced carbon-carbon plate. This example does not model a specific experiment; rather it was used to measure the improved computational efficiency of the method described here, in a hypervelocity impact application of current research interest [6,36]. The projectile material, diameter (0.618 cm), and impact velocity (7 km/s) represent a typical orbital debris impact threat [4], while the target plate thickness (0.47 cm) is characteristic of reinforced carbon-carbon components of the Space Shuttle thermal protection system [6]. Experimental studies of the mechanical properties of reinforced carbon-carbon are in progress; the material properties used in the simulations are listed in Table 6. A total of six simulations were performed, at three different particle counts, to measure the the computational cost of density calculations made using interpolations kernels, as compared to the nonholonomic formulation developed in the present paper. Each simulation was run to a stop time of ten microseconds, sufficient to perforate the target and include the shock loading and fragmentation processes of central interest in hypervelocity impact applications. Figures 10 through 15 show representative simulation results. Table 7 lists the wall clock times and processor

counts for the simulations, run on a Linux cluster composed of dual processor (3 GHz) nodes. The results show the relatively high computational cost of kernel based density calculations, in the present hybrid particle finite element context. Wall clock times are increased for all three problem sizes and associated processor counts, by an average factor of one third. This result is not surprising, since the finite element related portion of the computation is relatively inexpensive [22], while most of the particle related computations are performed in two sequential routines: one loops over all neighbor particles to determine the density, the second loops again over all neighbor particles to compute the particle interaction forces. The effect of introducing the nonholonomic density calculation developed here is to eliminate the first of these two routines. Considering the very high computational costs of three dimensional shock physics problems, the measured reduction in wall clock time is significant.

CONCLUSION

The present paper has formulated a new kernel free particle-finite element method and demonstrated its application in three dimensional hypervelocity impact simulations. Unlike alternative methods, the formulation is derived without reference to any weighting or interpolation functions for either the density or the rate of dilatation. The improved method introduces a new formulation of the thermomechanical Lagrange equations, one which employs internal energies as generalized coordinates. This avoids the requirement to perform certain Legendre transforms, in order to express the dependence of the pressure and temperature on entropy, and hence allows for the use of equations of state in standard form. As compared to the previous formulation, the revised method is both simplified and computationally more efficient. Applications work in progress is focused on the simulation of orbital debris impact effects on spacecraft thermal protection materials [6].

ACKNOWLEDGEMENTS

Table 1. Simulation parameters for the wall shock problem

Ratio of specific heats (γ)	$\frac{5}{3}$
Specific heat (c_v)	1.0
Reference internal energy (e_o)	1.0
Reference density (ρ_o)	1.0
Reference temperature (θ_o)	1.0
Numerical viscosity coefficient (c_o)	1.0
Numerical viscosity coefficient (c_1)	0.0
Numerical conduction coefficient (k_o)	0.1

Table 2. Error norms for the wall shock problem

Number of particles	Velocity error norm	Temperature error norm
100	0.17116	0.08594
200	0.12141	0.06075
400	0.08635	0.04325
800	0.06081	0.03032

Table 3. Simulation parameters for the bar impact problem

Length of the bar $(L$, in$)$	100
Bulk modulus $(K$, psi$)$	30.0×10^6
Applied end loading $(P_{ext}$, psi$)$	50.0×10^3
Reference density $(\rho_o$, pci$)$	0.73×10^{-3}
Numerical viscosity coefficient (c_o)	1.0
Numerical viscosity coefficient (c_1)	0.0

Table 4. Material properties used in the long rod impact simulations

Material property	Projectile	Target
Reference density (g/cc)	17.6	7.87
Shear modulus (Mbar)	1.45	0.801
Reference yield stress (Mbar)	0.0075	0.0105
Strain hardening coefficient	1.15	0.177
Strain hardening exponent	0.49	0.12
Thermal softening coefficient	1.0	1.0
Melt temperature (deg K)	1,700	1,723
Specific heat (Mbar-cm^3 per g-deg K)	0.143e-5	0.448e-5
Plastic failure strain	1.0	1.0

Table 5. Simulation results for the long rod impact problem

Number of particles	Residual length (cm)	Residual velocity (km/s)
35,992	6.08	1.42
92,498	6.47	1.42
187,826	6.59	1.42

Table 6. Material properties used in the plate impact simulations

Material property	Projectile	Target
Reference density (g/cc)	2.70	1.58
Shear modulus (Mbar)	0.271	0.0718
Reference yield stress (Mbar)	0.0029	0.000771
Strain hardening coefficient	125.0	2.0
Strain hardening exponent	0.10	1.0
Thermal softening coefficient	0.567	-1.0
Melt temperature (deg K)	1,220	3,840
Specific heat (Mbar-cm^3 per g-deg K)	0.884e-5	0.712e-5
Plastic failure strain	1.0	0.5

Table 7. Relative computational costs for the plate impact simulations

Particles	Density calculation	Processors	Wall clock hours	Relative cost
21,334	nonholonomic	4	1.2611	1.000
21,334	kernel	4	1.7581	1.394
63,253	nonholonomic	6	4.5047	1.000
63,253	kernel	6	5.8078	1.289
140,070	nonholonomic	8	28.8933	1.000
140,070	kernel	8	38.1411	1.320

REFERENCES

[1] Anderson CE, ed. Proceedings of the 2003 Hypervelocity Impact Symposium. *International Journal of Impact Engineering*, 2003; **29**: No. 1-10.

[2] Gisler G, Weaver R, Gittings M, and Mader C. Two and three dimensional asteriod ocean impact simulations. *International Journal of Impact Engineering*, 2003; **29**: 283-292.

[3] Knudson MD, Hall CA, Lemke R, Deeney C, and Asay JR. High Velocity Flyer Plate Launch Capability on the Sandia Z Accelerator. *International Journal of Impact Engineering*, 2003; **29**: 377-384.

[4] Hayhurst CJ, Livingstone IHG, Clegg, RA, Destefanis R, Faraud M. Ballistic limit evaluation of advanced shielding using numerical simulations. *International Journal of Impact Engineering*, 2001; **26**: 309-320.

[5] Yatteau JD, Recht GW, Edquits KT. Transverse loading and response of long rod penetrators during high velocity plate perforation. *International Journal of Impact Engineering*, 1999; **23**: 967-980.

[6] Christiansen EL and Friesen L. Penetration equations for thermal protection materials. *International Journal of Impact Engineering*, 1997; **20**: 153-164.

[7] Christiansen EL and Kerr JH. Projectile shape effects on shielding performance at 7 km/s and 11 km/s. *International Journal of Impact Engineering*, 1997; **20**: 165-172.

[8] Benson DJ. Computational methods in Lagrangian and Eulerian hydrocodes. *Computer Methods in Applied Mechanics and Engineering*, 1992; **99**: 235-394.

[9] McGlaun JM, Thompson SL, Elrick MG. CTH: A three dimensional shock wave physics code. *International Journal of Impact Engineering*, 1990; **10**: 351-360.

[10] Hertel ES. A COMPARISON OF THE CTH HYDRODYNAMICS CODE WITH EXPERIMENTAL DATA, 1992, SAND92-1879, Sandia National Laboratories.

[11] Hallquist JO. THEORETICAL MANUAL FOR DYNA3D, 1983, Lawrence Livermore National Laboratory, Livermore, California.

[12] Carroll DE, Hertel ES, Trucano TG. Simulation of armor penetration by tungsten rods: ALEGRA validation report, 1997, SAND97-2765, Sandia National Laboratories.

[13] Wallin BK, Tong C, Nichols AL, Chow ET. Large multiphysics simulations in ALE3D. Presented at the Tenth SIAM Conference on Parallel Processing for Scientific Computing, Portsmouth, Virginia, March 12-14, 2001.

[14] Stellingwerf RF, Wingate CA. Impact modeling with smooth particle hydrodynamics. *International Journal of Impact Engineering*, 1993; **14**: 707-718.

[15] Shapiro PR, Martel H, Villumsen JV, Owen JM. Adaptive smoothed particle hydrodynamics with application to cosmology: methodology. *The Astrophysical Journal Supplement Series*, 1996; **103**: 269-330.

[16] Owen JM, Villumsen JV, Shapiro PR, Martel H. Adaptive smoothed particle hydrodynamics with application to cosmology: methodology II. *The Astrophysical Journal Supplement Series*, 1998; **116**: 155-209.

[17] Belytschko T, Krongauz Y, Organ D, Fleming M, Krysl P. Meshless methods: an overview and recent developments. *Computer Methods in Applied Mechanics and Engineering*, 1996; **139**: 3-47.

[18] Fahrenthold EP. Numerical simulation of impact on hypervelocity shielding. Proceedings of the Hypervelocity Shielding Workshop, 1998, Galveston, Texas, pp. 47-50.

[19] Fahrenthold EP, Horban BA. An improved hybrid particle-element method for hypervelocity impact simulation. *International Journal of Impact Engineering*, 2001; **26**: 169-178.

[20] Johnson GR, and Stryk RA. Conversion of 3D distorted elements into meshless particles during dynamic deformation. *International Journal of Impact Engineering*, 2003; **28**: 947-966.

[21] Shivarama R and Fahrenthold EP. An ellipsoidal particle-finite element method for hypervelocity impact simulation. *International Journal for Numerical Methods in Engineering*, 2004; **59**: 737-753.

97

[22] Fahrenthold EP, Shivarama R. Extension and validation of a hybrid particle-element method for hypervelocity impact simulation. *International Journal of Impact Engineering*, 2003; **29**: 237-246.

[23] Haim Baruh. ANALYTICAL DYNAMICS, 1999, McGraw Hill, New York.

[24] Rapaport DC. Molecular dynamics simulation using quaternions. *Journal of Computational Physics*, 1985; **41**: 306-314.

[25] Lubliner J. PLASTICITY THEORY, 1990, Macmillan, New York

[26] Lyon SP, Johnson JD, editors. SESAME: THE LOS ALAMOS NATIONAL LABORATORY EQUATION OF STATE DATABASE, LA-UR-92-3407, Los Alamos National Laboratory, Los Alamos, New Mexico.

[27] Fahrenthold EP, Horban BA. Thermodynamics of continuum damage and fragmentation models for hypervelocity impact. *International Journal of Impact Engineering*, 1997; **20**: 241-252.

[28] Silling SA. CTH REFERENCE MANUAL: JOHNSON-HOLMQUIST CERAMIC MODEL, 1992, SAND92-0576, Sandia National Laboratories.

[29] Liden E, Ottosson J, and Holmberg L. WHA rods penetrating stationary and moving oblique steel plates. Proceedings of the 16th International Symposium on Ballistics, 1996, pp. 711-719.

[30] Lee M, Yoo YH. Assessment of a new dynamic FE-Code: application to the impact of a yawed-rod onto nonstationary oblique plate. *International Journal of Impact Engineering*, 2003; **29**: 425-436.

[31] Noh, W.F. Errors for calculation of strong shocks using an artificial viscosity and an artificial heat flux. *Journal of Computational Physics*, 1978; **72**: 78-120.

[32] Steinberg DJ. EQUATION OF STATE AND STRENGTH PROPERTIES OF SELECTED MATERIALS, 1996, Lawrence Livermore National Laboratory, UCRL-MA-106439.

[33] Kolsky H. STRESS WAVES IN SOLIDS, 1963, Dover, New York

[34] Lu, YY, Belytschko, T, and Tabbara, M.. Element-free Galerkin method for wave propagation and dynamic fracture. *Computer Methods in Applied Mechanics and Engineering*, 1995; **126**: 131-153.

[35] Fahrenthold, EP, and Koo, JC. Discrete Hamilton's equations for viscous compressible fluid dynamics. *Computer Methods in Applied Mechanics and Engineering*, 1999; **178**: 1-22.

[36] Fahrenthold, EP, and Park, YK. Simulation of foam impact effects on the space shuttle thermal protection system. *AIAA Journal of Spacecraft and Rockets*, in press.

LIST OF FIGURES

Figure 1: Wall shock problem, velocity versus position at t = 0.3.
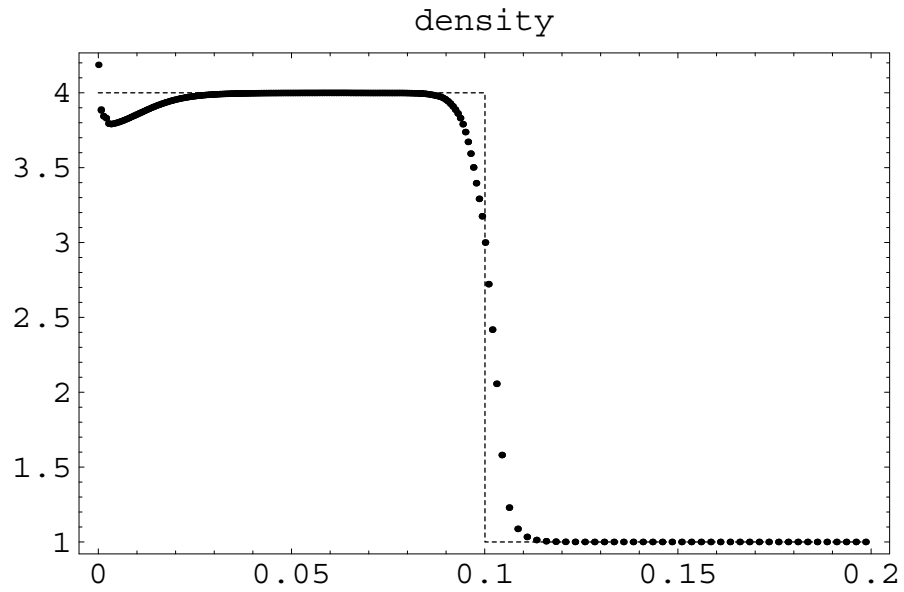
Figure 2: Wall shock problem, density versus position at t = 0.3.
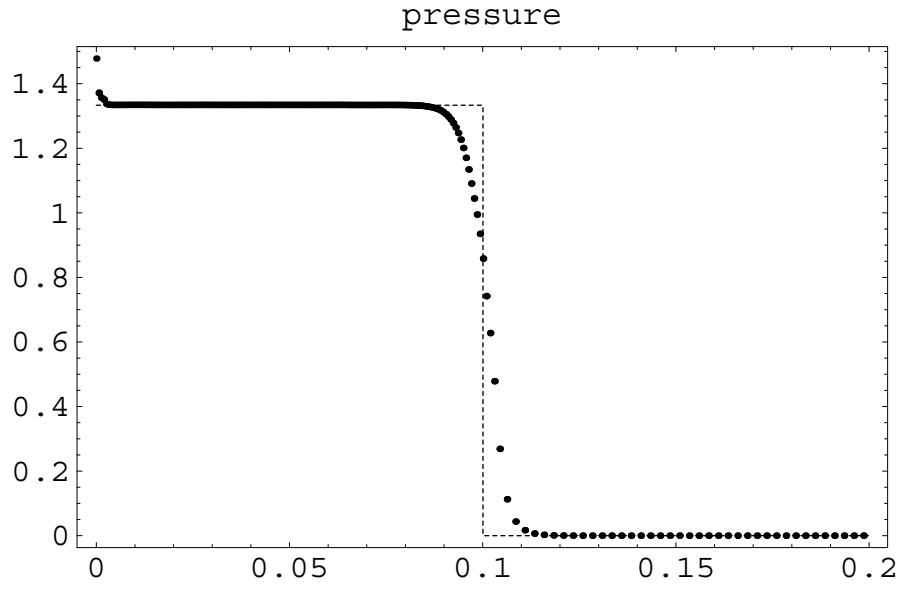
Figure 3: Wall shock problem, pressure versus position at t = 0.3.
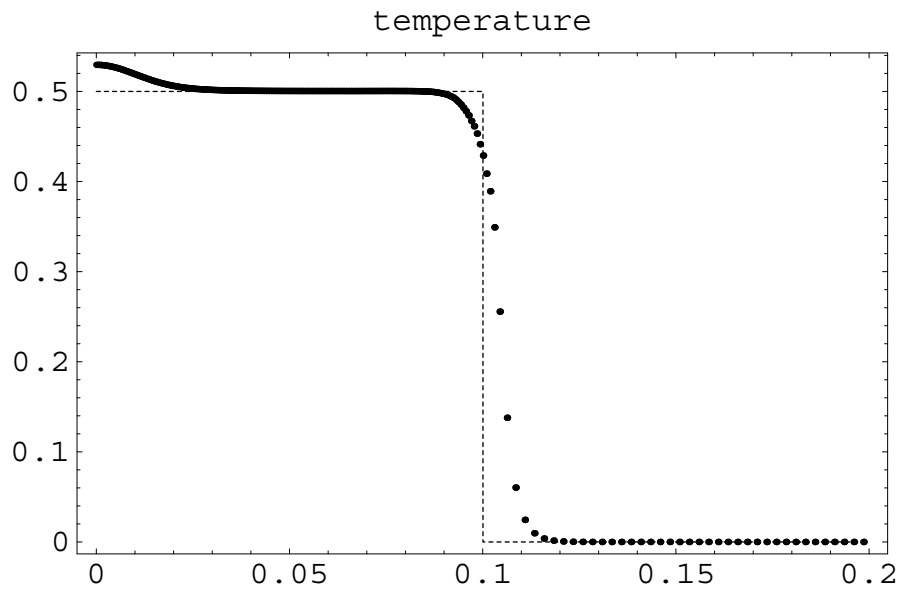
Figure 4: Wall shock problem, temperature versus position at t = 0.3.
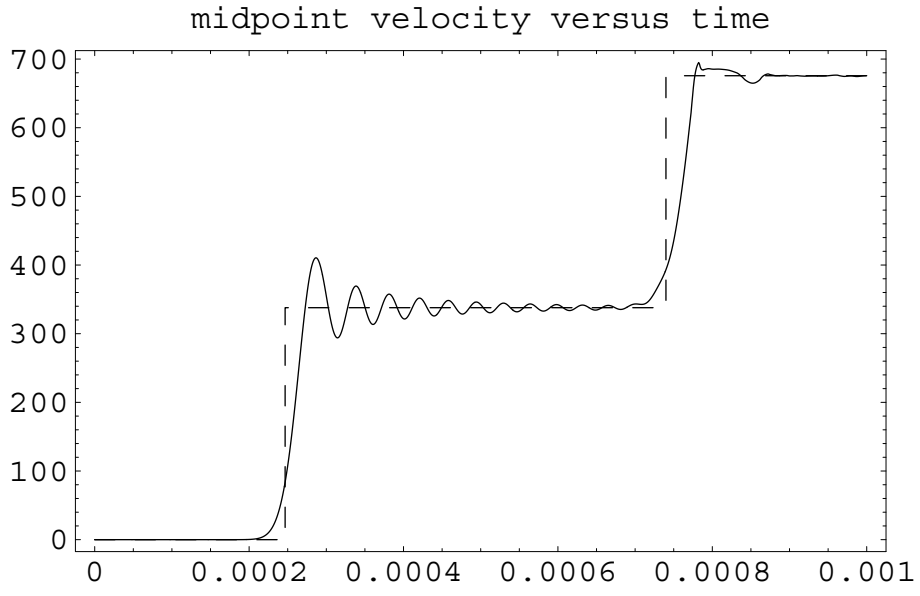
Figure 5: Bar impact problem, midpoint velocity versus time for 51 particles.
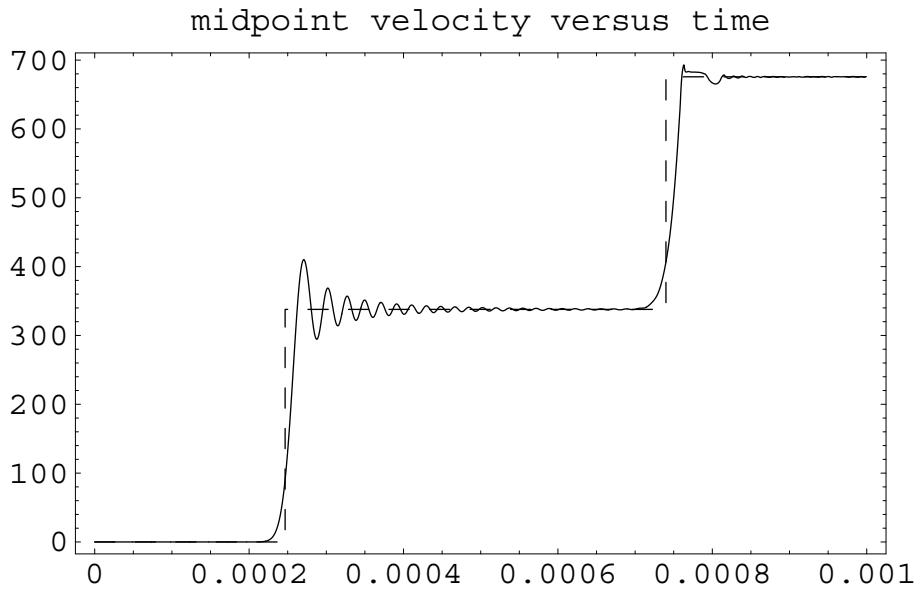
Figure 6: Bar impact problem, midpoint velocity versus time for 101 particles.

103
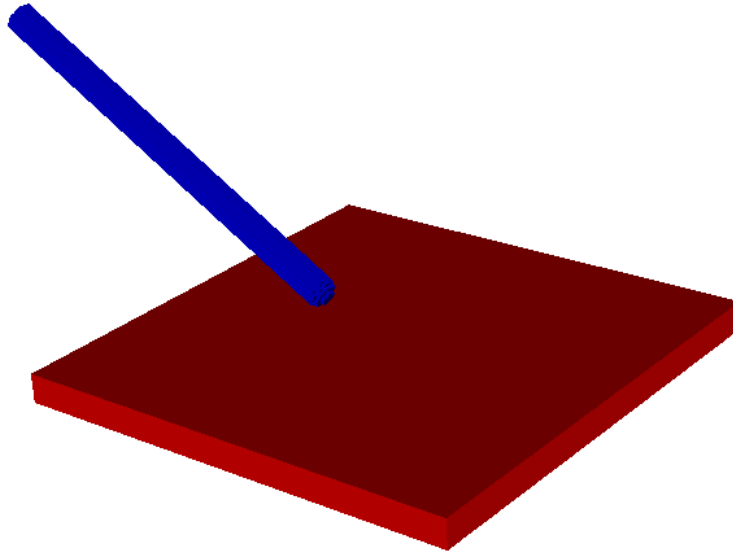
Figure 7: Long rod impact problem, element plot of the initial configuration.
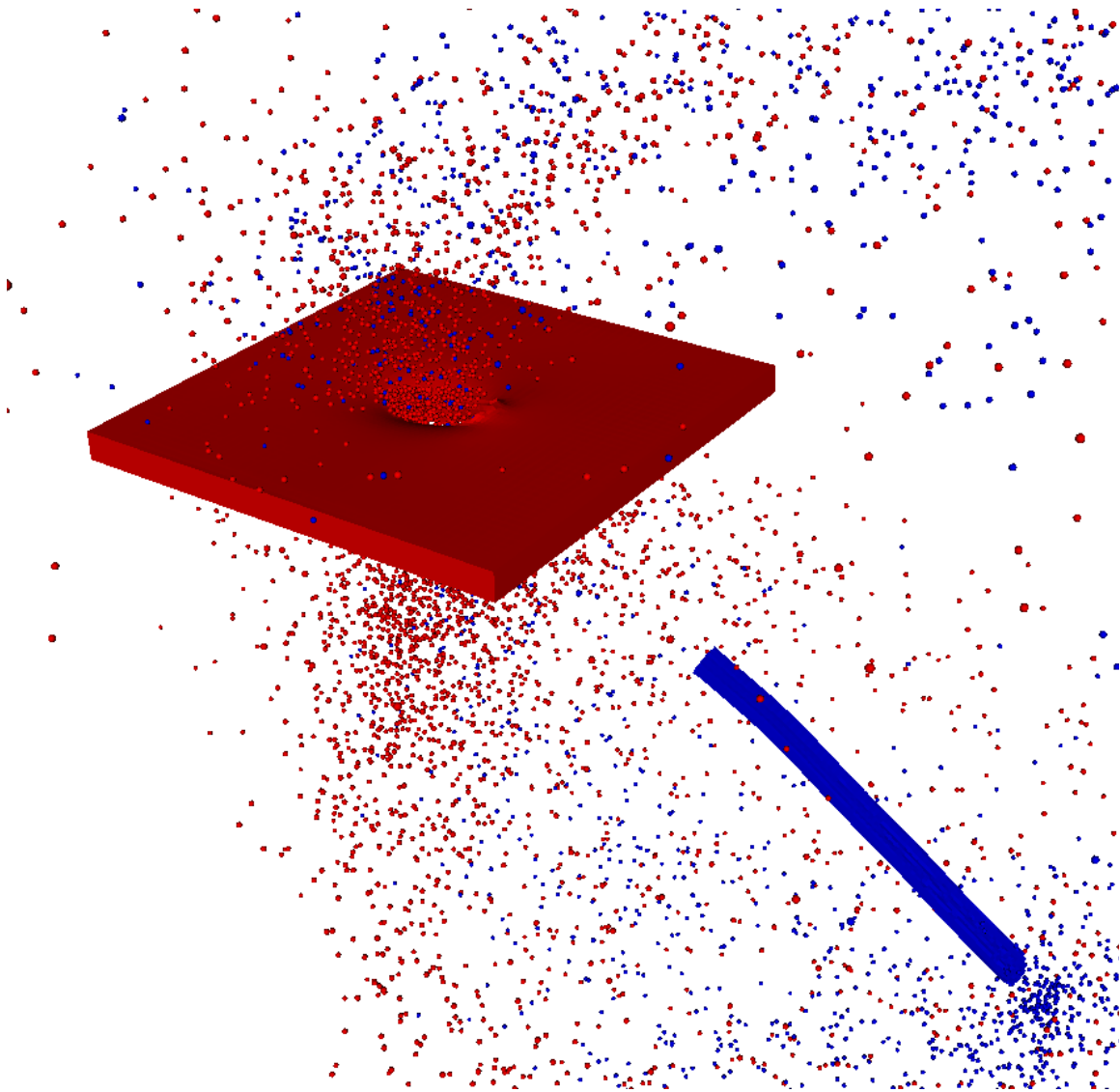
Figure 8: Long rod impact problem, particle-element plot at 100 microseconds after impact.
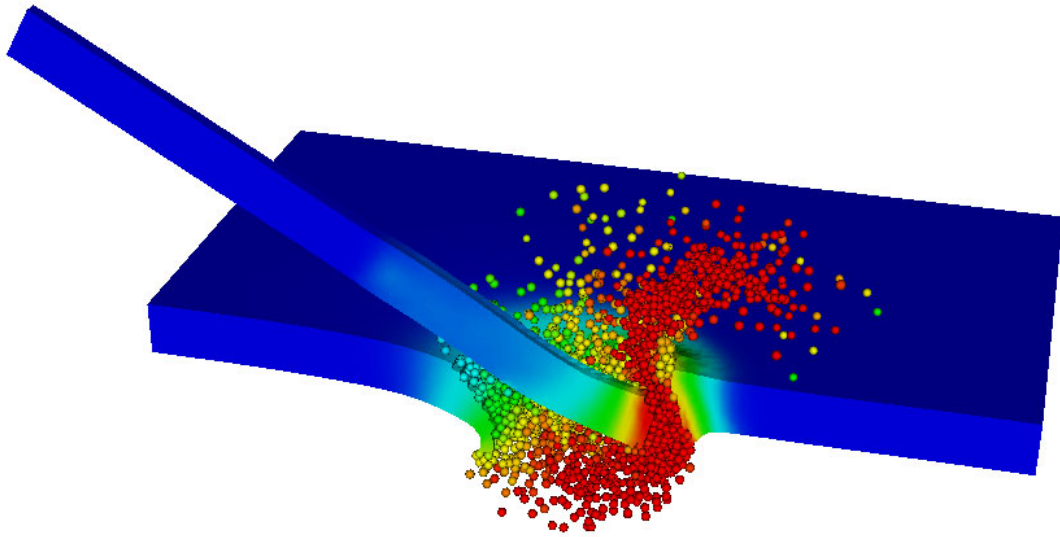
Figure 9: Long rod impact problem, sectioned particle-element plot at 20 microseconds after impact, color on temperature.
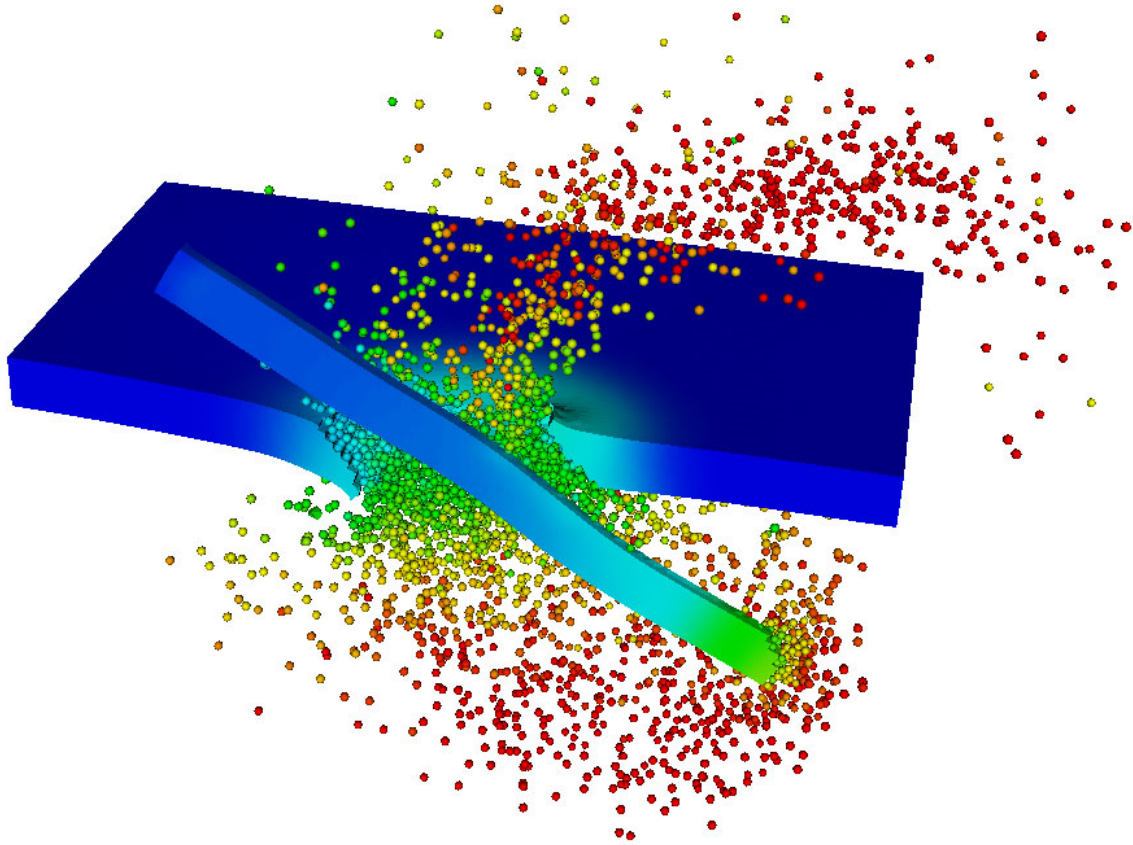
Figure 10: Long rod impact problem, sectioned particle-element plot at 40 microseconds after impact, color on temperature.
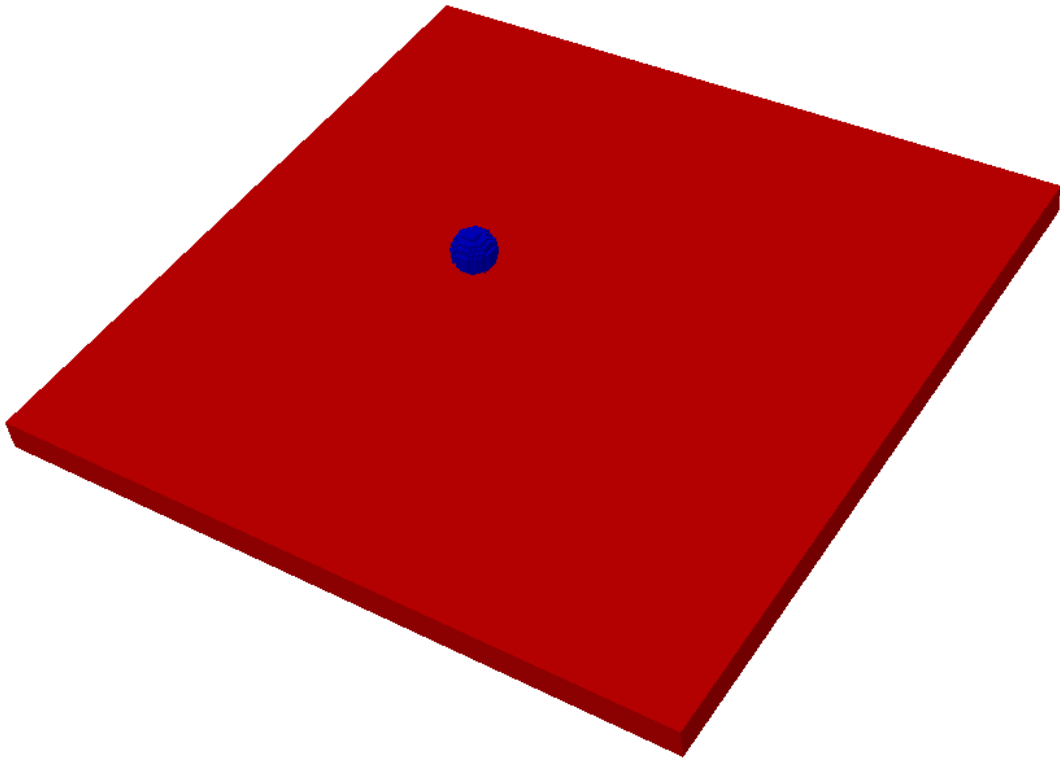
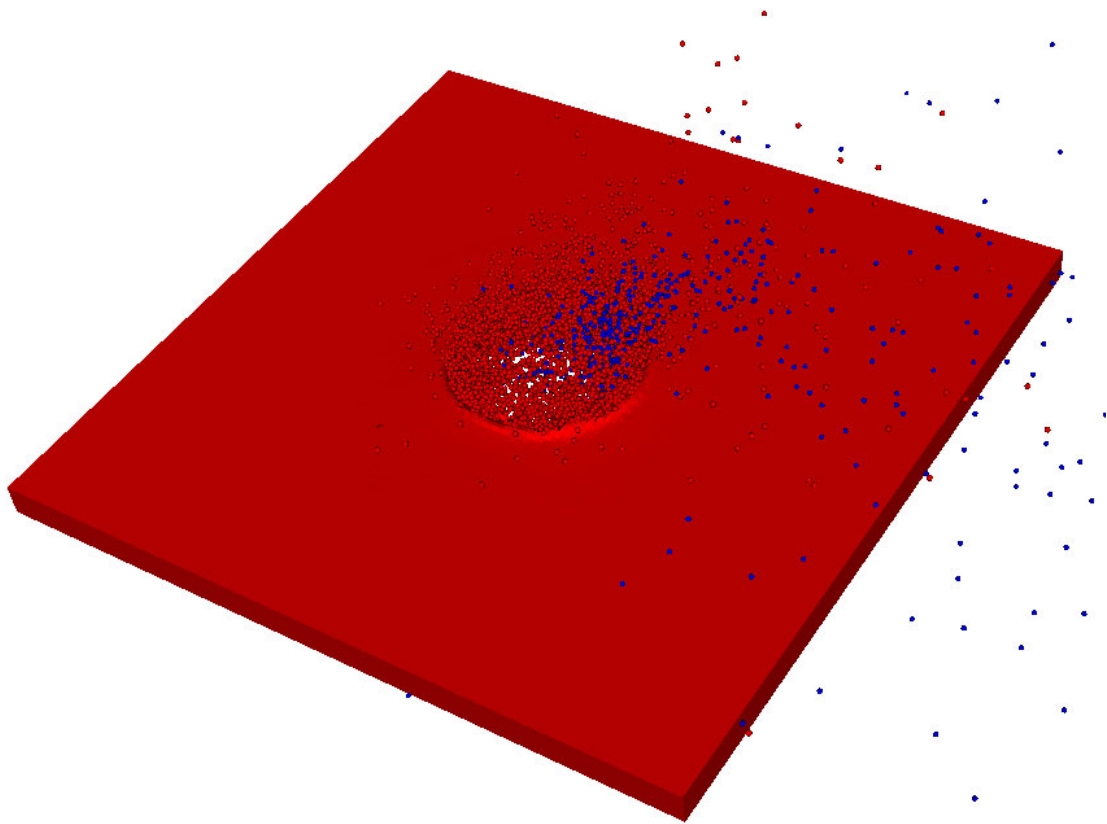Figure 11: Plate impact problem, element plot of the initial configuration.

Figure 12: Plate impact problem, particle-element plot at 10 microseconds after impact.
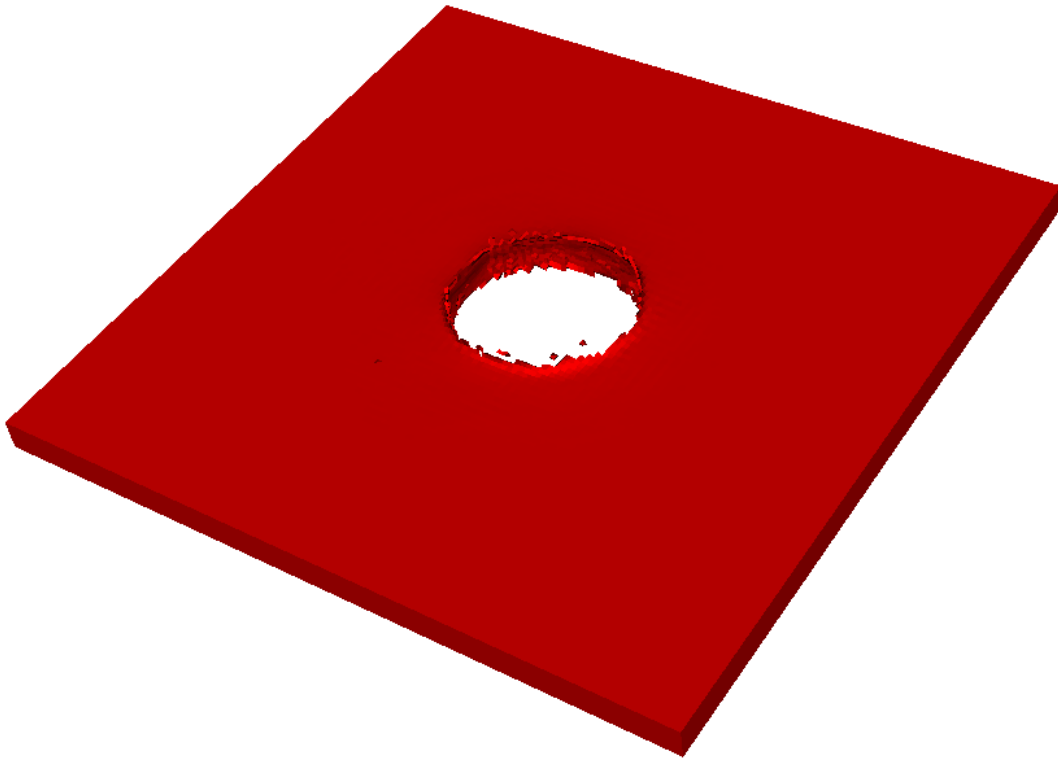
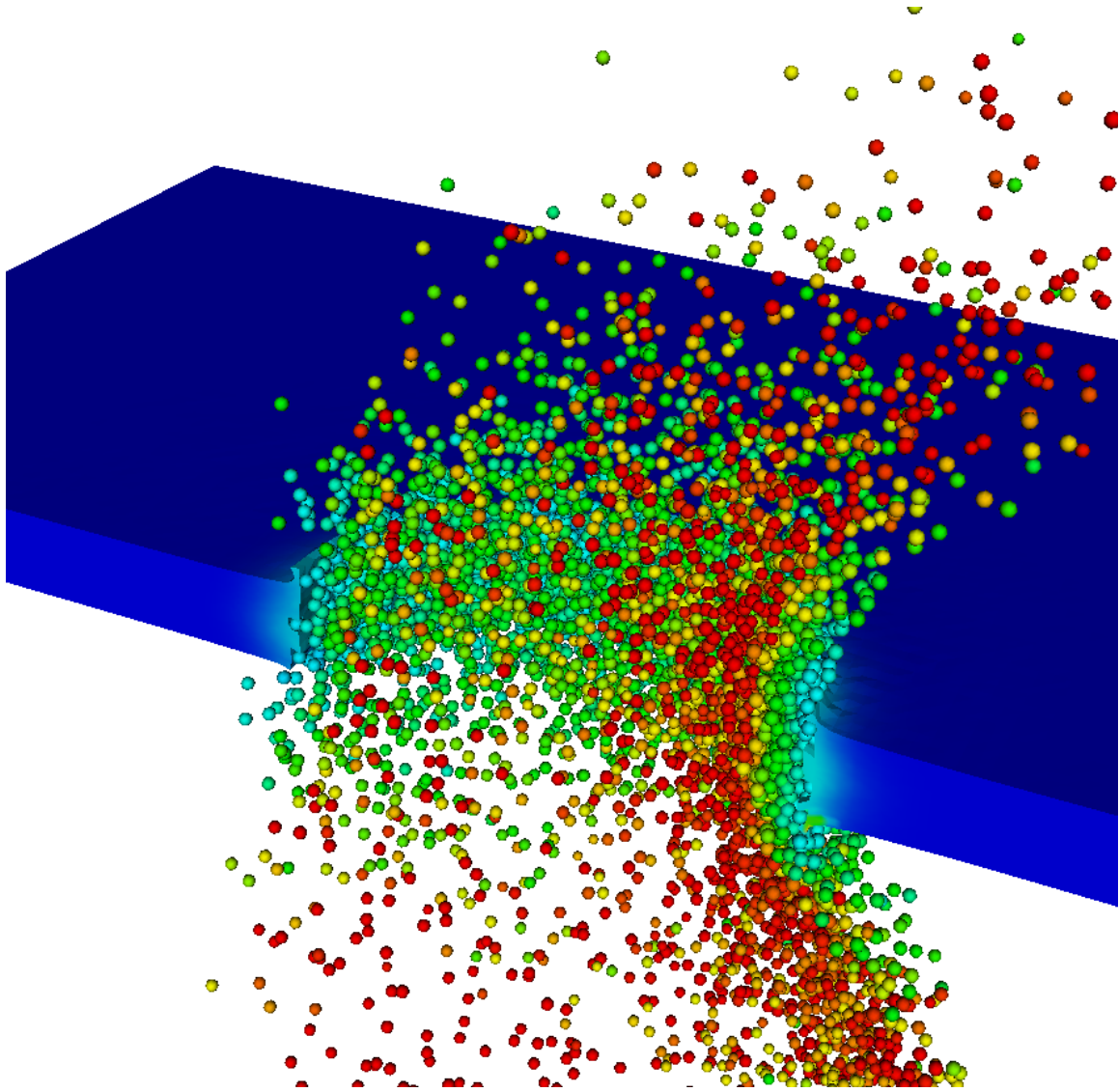Figure 13: Plate impact problem, element plot at 10 microseconds after impact.

Figure 14: Plate impact problem, sectioned particle-element plot at 10 microseconds after impact, color on temperature.
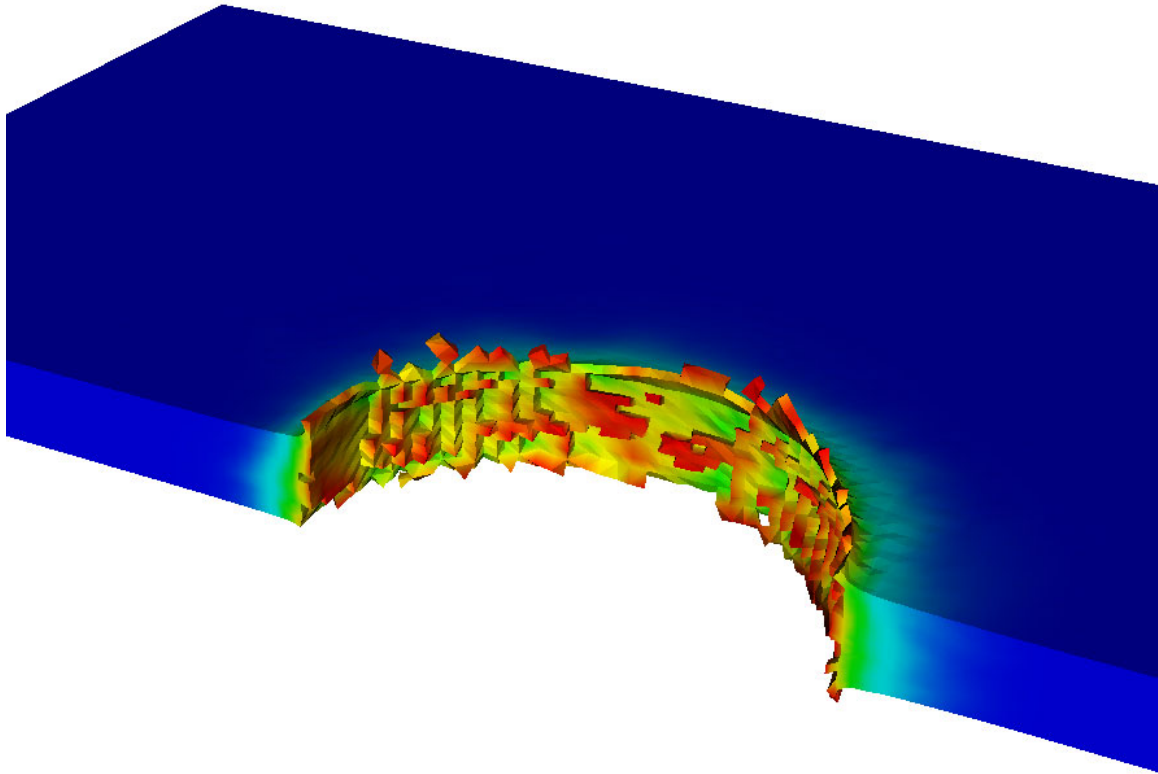
Figure 15: Plate impact problem, sectioned element plot at 10 microseconds after impact, color on effective plastic strain.